Nonlinear simulation of resistive ballooning modes in the Large Helical Device

Nonlinear simulation of resistive ballooning modes in the Large Helical Device

Hideaki Miura, Takaya Hayashi, and Tetsuya Sato
Theory and Computer Simulation Center, National Institute for Fusion Science, Oroshi 322-6, Toki, Gifu 509-5292, Japan

(Received 2 May 2001; accepted 13 August 2001)

Nonlinear simulations of a magnetohydrodynamic (MHD) plasma in full three-dimensional geometry of the Large Helical Device (LHD) [O. Motojima *et al.*, Phys. Plasmas **6**, 1843 (1999)] are conducted. A series of simulations shows growth of resistive ballooning instability, for which the growth rate is seen to be proportional to the one-third power of the resistivity. Nonlinear saturation of the excited mode and its slow decay are observed. Distinct ridge/valley structures in the pressure are formed in the course of the nonlinear evolution. The compressibility and the viscous heating, as well as the thermal conduction, are shown to be crucial to suppress the pressure deformations. Indication of a pressure-driven relaxation phenomenon that leads to an equilibrium with broader pressure profile is observed. © *2001 American Institute of Physics.* [DOI: 10.1063/1.1408624]

I. INTRODUCTION

This paper is concerned with an attempt to run a nonlinear magnetohydrodynamic (MHD) simulation of a helical plasma that is executed in a full three-dimensional (3D) geometry. In particular, the behavior of plasma is studied for the Large Helical Device (LHD) configuration.[1] The LHD system is a heliotron/torsatron type helical device with a plane magnetic axis with two helical coils, where the pitch period number $M=10$ and the aspect ratio of the major radius to the average minor radius of a plasma is 6.5. A series of experimental programs using the LHD are now under way and some successful results have been reported.[2] Since macro-scale plasma fluctuations in the LHD system are considered to be dominated by pressure-driven instabilities, understanding of linear and nonlinear behaviors of these kinds of instabilities is important to achieve good confinement. Although nonlinear behaviors of a MHD plasma have been extensively investigated for tokamak plasmas (see Mizuguchi *et al.*,[3] for example), little is known about helical plasmas.

Here we concentrate on a MHD plasma to study pressure-driven instabilities in helical systems. This kind of instability is often investigated through linear stability analysis and/or numerical simulations of reduced MHD equations. One of the most successful approaches of stability analysis is the stellarator expansion method, which was introduced by Greene and Johnson,[4] as well as the averaging method. There are an enormous number of works which employ these methods to analyze MHD linear stability of helical plasmas.[5,6]

While linear stability analysis by means of the stellarator expansion method is essentially two-dimensional, there is three-dimensional analysis, too.[7,8] Furthermore, recent numerical codes such as CAS3D[9] and TERPSICHORE[10] are used to investigate the linear stability of three-dimensional heliotron equilibria.

We have to note that development of the stability codes, such as CAS3D and TERPSICHORE, has permitted the analysis of three-dimensional instability with low-n modes, where n denotes the toroidal Fourier mode number. Most of the previous research on linear analysis has been dedicated to ideal MHD instabilities, and the properties of a resistive MHD instabilities remain unclarified. (Development of a 3D resistive linear code has been reported recently.[11]) On the other hand, some experimental results suggest that plasma behaviors are often dominated by resistive instabilities for low-n modes. For example, Sakakibara *et al.*[12] have reported that the growth of the resistive interchange mode was as important as the ideal interchange mode in their Compact Helical System (CHS) experiment.

Nonlinear investigations of helical systems have been conducted by making use of reduced MHD equations, which were first derived by Strauss.[13] There are several works using reduced MHD equations,[14–16] which have successfully treated low-n modes concerning internal disruption phenomena. However, fully three-dimensional structures had to be out of the scope of this research because, from derivation, the reduced MHD systems could express effects of the three-dimensional helical magnetic structure only in an averaged manner. Thus, behaviors of ideal or resistive ballooning modes that strongly depend on local magnetic curvature effects have not yet been understood.

In an attempt to investigate the complex nonlinear behaviors of a MHD plasma in a three-dimensional structure, we have to execute fully three-dimensional MHD simulations without employing specific approximations for the structure. For this purpose, we have developed a new simulation code, which solves a full set of MHD equations in a fully three-dimensional toroidal geometry. This simulation code is a natural extension of the HINT code,[17] which obtains a fully three-dimensional equilibrium state without imposing the nested flux assumption. Based on a preliminary trial of the code development,[18] the nonlinear simulation code has been improved to include effects of the shear viscosity and to treat a full-torus system. We aim to understand the nonlinear

behaviors of an MHD plasma in a helical system by making use of the newly developed code. The main target of our investigation is to study evolution and saturation of pressure-driven instabilities, which grow in the currentless equilibria of helical plasmas. Another basic motivation of this study is to see whether or not the growth of mild pressure-driven instabilities can cause a kind of a relaxation process, namely, a transition from an initial excessive energy state to a stable state that a plasma chooses through redistribution of the plasma pressure. We emphasize that nonlinear investigation of helical MHD plasma including fully three-dimensional structures has seldom been attempted. There is not much knowledge of nonlinear behaviors of helical plasmas. Although our code can treat low-n (fully toroidal) modes by solving the entire toroidal system, such a full-torus simulation is expensive in terms of computation time. As a first step in the attempt to execute simulations in three-dimensional geometry, we impose the stellarator symmetry in this paper. We assume that some basic nature of the nonlinear behavior of pressure-driven instabilities can be observed even in this restricted situation. Actually, as shown in Sec. III, an indication of a relaxation phenomenon caused by the nonlinear evolution of mild unstable modes is found.

This paper is organized as follows. Section II provides outlines of our simulations. Basic equations, boundary conditions, and the discretization scheme are described there. We also describe how to give an initial condition. Section III presents the results of nonlinear simulations. Some observations in the linear and nonlinear regimes are described there. Concluding remarks are in Sec. IV.

II. OUTLINE OF SIMULATION SCHEMES

A. MHD equations and boundary conditions

We solve the time evolution of a full set of nonlinear, compressible, nonideal (dissipative) MHD equations

$$\frac{\partial \rho}{\partial t} = -\frac{\partial}{\partial x_i}(\rho V_i), \tag{1}$$

$$\frac{\partial(\rho V_i)}{\partial t} + \frac{\partial}{\partial x_j}(\rho V_i V_j) = -\frac{\partial p}{\partial x_i} + \epsilon_{ijk} J_j B_k + \mu\left[\frac{\partial^2 V_i}{\partial x_j \partial x_j} + \frac{1}{3}\frac{\partial}{\partial x_i}\left(\frac{\partial V_j}{\partial x_j}\right)\right], \tag{2}$$

$$\frac{\partial p}{\partial t} + V_j \frac{\partial p}{\partial x_j} = -\gamma p \frac{\partial V_j}{\partial x_j} + (\gamma - 1) \times \left[\eta J_j J_j + \Phi - \frac{\partial}{\partial x_j}\left(-\kappa \frac{\partial}{\partial x_j}\frac{p}{\rho}\right)\right], \tag{3}$$

$$\frac{\partial B_i}{\partial t} = -\epsilon_{ijk}\frac{\partial}{\partial x_j}(-\epsilon_{klm} V_l B_m + \eta J_k), \tag{4}$$

$$J_i = \epsilon_{ijk}\frac{\partial B_k}{\partial x_j}, \tag{5}$$

$$\Phi = 2\mu\left[e_{ij}e_{ji} - \frac{1}{3}\left(\frac{\partial V_i}{\partial x_i}\right)\left(\frac{\partial V_j}{\partial x_j}\right)\right], \tag{6}$$

$$e_{ij} = \frac{1}{2}\left(\frac{\partial V_i}{\partial x_j} + \frac{\partial V_j}{\partial x_i}\right). \tag{7}$$

The symbols V_i, B_i, J_i and e_{ij} are ith components of the velocity vector, magnetic field vector, current vector and (i,j) component of the rate-of-strain tensor in the Cartesian coordinate, respectively. The symbols ρ and p represent the density and pressure, respectively. The symbol ϵ_{ijk} represents Edington's anti-symmetric tensor. We take a sum from 1 to 3 on repeated suffices. The conductivity, resistivity, and shear viscosity are represented by κ, η and μ, respectively. Equations (1)–(7) are already nondimensionalized by using the characteristic toroidal magnetic field B_0, the toroidal Alfvén velocity $V_a = B_0/\sqrt{\mu_0 \rho_0}$ defined by using B_0, the permeability μ_0 and characteristic density ρ_0, and the characteristic length L_0. The geometry is set to simulate the LHD configuration. The dissipative coefficients κ, η, and μ are assumed to be constant and isotropic in our simulations so that we start from the simplest model.

The MHD equations (1)–(7) are now described in the helical-toroidal coordinate system (u^{1*}, u^2, u^3), which has been adopted in the HINT code.[17] The toroidal-helical coordinate system (u^{1*}, u^2, u^3) used here is described as

$$u^{1*} = u^1 + \delta = r\cos(\theta - h\phi), \tag{8}$$

$$u^2 = r\sin(\theta - h\phi), \tag{9}$$

$$u^3 = -\phi, \tag{10}$$

by the minor radius of the torus r, distance from the origin of the coordinate system δ, the poloidal angle θ and the toroidal angle ϕ; see Fig. 1 in Harafuji *et al.*[17] on the coordinate system. Since we aim to study a MHD plasma in the LHD geometry, we set $\delta = 0$ and a set of values $M = 10$ and $h = M/2$ is adopted throughout this article. The MHD equations in this coordinate system are described in Appendix A. We impose the stellarator symmetry to this system. The stellarator symmetry consists of $M = 10$ periodic boundary condition on one-pitch period and a sort of symmetric condition on the magnetic field at $\phi = 0$ and at the middle of the one-pitch period $\phi = \pi/M$. Boundary conditions on the density, pressure, and velocity fields are determined so that the MHD equations (1)–(7) are invariant when the boundary condition is imposed on the magnetic field. Then, the toroidal mode number available in our simulation is multiples of 10, when the mode number is measured in a full-torus geometry. See Appendix B for details of the toroidal boundary conditions in our coordinate system.

In Fig. 1, the computational domain is drawn in a gray, twisted rectangular box. The computational domain covers a half-pitch period in the toroidal (u^3) direction. The plasma is assumed to be surrounded by a perfectly conducting wall. A pair of helically twisted coils of the LHD device and a typical isosurface of the plasma pressure are drawn for the readers' convenience to understand the symmetry. The pressure profile used to draw the isosurface is a result of a nonlinear simulation which will be described in the next section. It is seen that the overall pressure profile is twisted ten times in the toroidal direction.

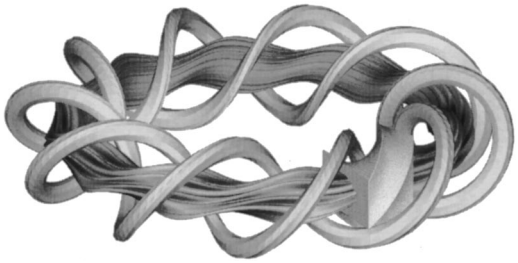

FIG. 1. Computational domain, LHD coils and an isosurface of the pressure. A gray, twisted rectangular box represents the computational domain in which an MHD plasma is simulated in our simulations. The box has half-pitch period in the toroidal direction. LHD coils and an isosurface of the pressure obtained in our simulation are drawn in fully toroidal geometry.

Equations (1)–(7) are discretized uniformly in the helical-toroidal coordinate system (u^{1*}, u^2, u^3) and the spatial differences are evaluated by the fourth-order central-finite-difference scheme. The resultant discrete equations are marched by the Runge–Kutta–Gill method, which has fourth-order accuracy in time. The number of grid points in the u^1, u^2, u^3 directions are represented as N_1, N_2 and N_3, respectively. Here N_3 is a grid number for the half-period in the toroidal direction. We have conducted simulations with $N_1=N_2=49, N_3=16$ (lower-resolution), $N_1=N_2=97, N_3=32$ (medium-resolution), and $N_1=N_2=193, N_3=32$ (higher-resolution). We have confirmed the soundness of the computations by checking that no significant difference appears in the structure of the fluctuation and the process of the mode growth between the medium- and higher-resolution computations. Here we report our numerical results with the medium- and higher-resolutions.

When we discretize the nonlinear equations to solve them numerically, numerical errors inevitably emerge, which are often called aliasing errors (see text by Roache,[19] for example). Removal of aliasing errors is simple and easy when we impose periodic boundary conditions on the system because we only have to operate a low-pass filter to the variables, as is often adopted by well-known spectral methods.[20] The cutoff wave number of a low-pass filter must be decided by investigating the nonlinearity of the equations to be solved. However, it is not the case in this article because boundary conditions in the u^{1*} and u^2 directions are not periodic. Instead of having a clearcut de-aliasing by using a low-pass filtering operation, here we make use of a smoothing scheme by taking the weighted-average of variables at neighboring grid points.[21] The scheme was adopted by Mizuguchi *et al.*[3] in their three-dimensional MHD simulations of a spherical tokamak, to show satisfactory results. This scheme contributes not only to the removal of aliasing errors but to the stabilizing of the discretized system. Note that relatively large-scale structures have the most unstable nature under the parameters used in this paper. Then the de-aliasing smoothing operation works only to remove small numerical oscillations and does not change the physical picture of the numerical results.

B. An initial equilibrium obtained by using the HINT code

An initial equilibrium is prepared using the HINT code.[17] The HINT code makes use of a relaxation scheme to obtain an ideal MHD equilibrium. In the HINT code, an initial pressure profile is given by

$$p(\psi)=(1-\psi^a)^b, \tag{11}$$

where ψ represents an initial toroidal flux function. Parameters a and b controls the initial profile of the pressure. Here a set of parameters $a=1$ and $b=2$ is adopted. The choice of parameters is the same as those of Ichiguchi *et al.*[22] who studied the Mercier stability of the LHD system by using the VMEC code.[23] We study a case where the major radius of the vacuum magnetic axis R_{ax} is located at $R_{ax}=3.7$ m in the real dimension. This case corresponds to a case where the vacuum axis is slightly inwardly shifted. (The center of the helical coil for LHD is located at 3.9 m in the major radius.) In this paper, we restrict ourselves to an initial equilibrium whose central beta β_0 is 4%. According to a previous study,[22] a part of magnetic surfaces for an equilibrium with $R_{ax}=3.7$ m and $\beta_0=4\%$ is analyzed to be unstable for the Mercier criterion.

In Figs. 2(a) and 2(b), Poincare plots of the magnetic field lines on horizontally and vertically elongated poloidal sections at $\phi=0$ and $\phi=\pi/M$, respectively, are shown. Hereafter, in figures of Poincare plots and contour plots, the right-hand side represents the outer side of the torus both for the horizontally or vertically elongated cross-sections. We see in Figs. 2(a) and 2(b) that the Shafranov shift has put the position of the magnetic axis toward the outer side of the torus. Consequently, the magnetic axis is observed relatively in the right-hand side in Figs. 2(a) and 2(b). In Fig. 2(c), the profile of the rotational transform $\iota/2\pi$ is shown. The abscissa represents the averaged minor radius. In Fig. 2(d) a bird's-eye view of the pressure on a poloidal section is shown. It is seen that the pressure has a clear bell-shape, which is a natural result of the parameter set $a=1, b=2$ for the initial pressure profile of the HINT code. In Fig. 2(e), a bird's-eye view of the toroidal current on the same poloidal section as Fig. 2(d) is shown. It is seen that the Pfirsch–Schlüter current is emerging on the center of the poloidal section, keeping the net toroidal current null.

Note here that the HINT code does not necessarily provide a linearly stable equilibrium. Since dynamics of the pressure perpendicular to the magnetic field lines is excluded in the HINT computation, the HINT equilibrium can be unstable, especially with an interchange or a ballooning instability. In simulations with an initial equilibrium as shown in Figs. 2, an instability is driven by the pressure gradient due to its unstable nature.

III. SIMULATION RESULTS

A. Growth of a resistive ballooning instability

Now we investigate time evolution of the MHD equations (1)–(7). In what follows, the conductivity $\kappa=1\times10^{-6}$ is fixed throughout this article. So far as we do not

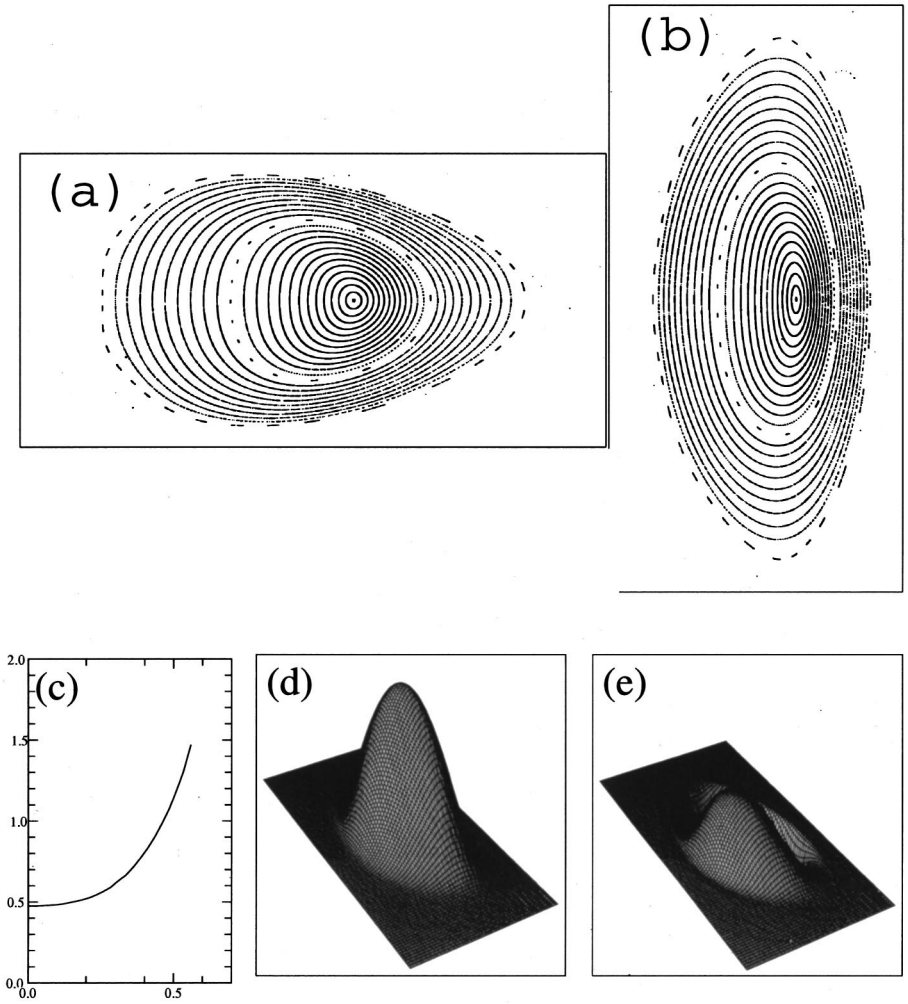

FIG. 2. Profiles of an initial equilibrium state obtained by the HINT code. Poincare plots of magnetic lines on a horizontally and vertically elongated poloidal sections, $\phi=0$ and π/M are shown in (a) and (b), respectively. The rotational transform $\iota/2\pi$ is shown in (c). Birds'-eye views of the pressure and toroidal current on a poloidal section are shown in (d) and (e), respectively.

describe explicitly, the resistivity η and the shear viscosity μ are 3.16×10^{-6} and 2×10^{-3}, respectively. A simulation with this parameter set is conducted with the higher-resolution computation.

In Fig. 3, time evolutions of the kinetic energies obtained by the typical three simulations, $\eta=1\times10^{-6}$, 1.78×10^{-6} and 3.16×10^{-6} are shown. The vertical axis is plotted in log-scale. The origin of the abscissa is set to the time just before an exponential growth. In order to see plasma behaviors in the exponential growth period, we concentrate on a simulation with $\eta=3.16\times10^{-6}$ and observe pressure deformations. Contour plots of the pressure on horizontally and a vertically elongated poloidal sections at $t=200\tau_A$ are shown, respectively, in Figs. 4(a) and 4(b). There are some deformations of the pressure contours on the outer side of the torus. The nature of these deformations is shown in Figs. 4(c) and 4(d) by contour plots of the amplitude of the pressure fluctuation on the horizontally and vertically elongated poloidal sections at $t=200\tau_A$, respectively. We see that the pressure fluctuation is localized around a circular region where the pressure gradient is the steepest. The fluctuation is especially large on the outer side of the torus. Note that the destabilization effect of the magnetic curvature becomes strongest on the outer side of the horizontally elongated poloidal section for the heliotron type helical configuration. These observations suggest that the exponential growth is caused by a ballooning instability. It is considered that a weak interchange instability also contributes to the pressure deformations because there are small deformations on the inner side of the torus. (Recall that our initial equilibrium solution is expected to be Mercier-unstable.) As time proceeds, wavy

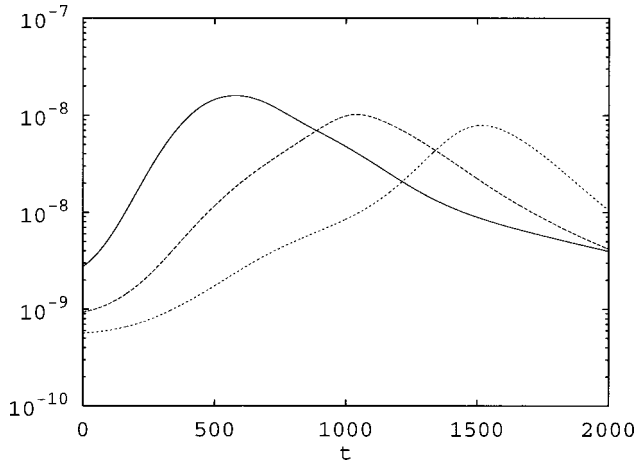

FIG. 3. Time evolution of the kinetic energy. Solid, dashed and dotted lines represent runs with the resistivity $\eta=3.16\times10^{-6}$, 1.78×10^{-6}, 1×10^{-6}, respectively.

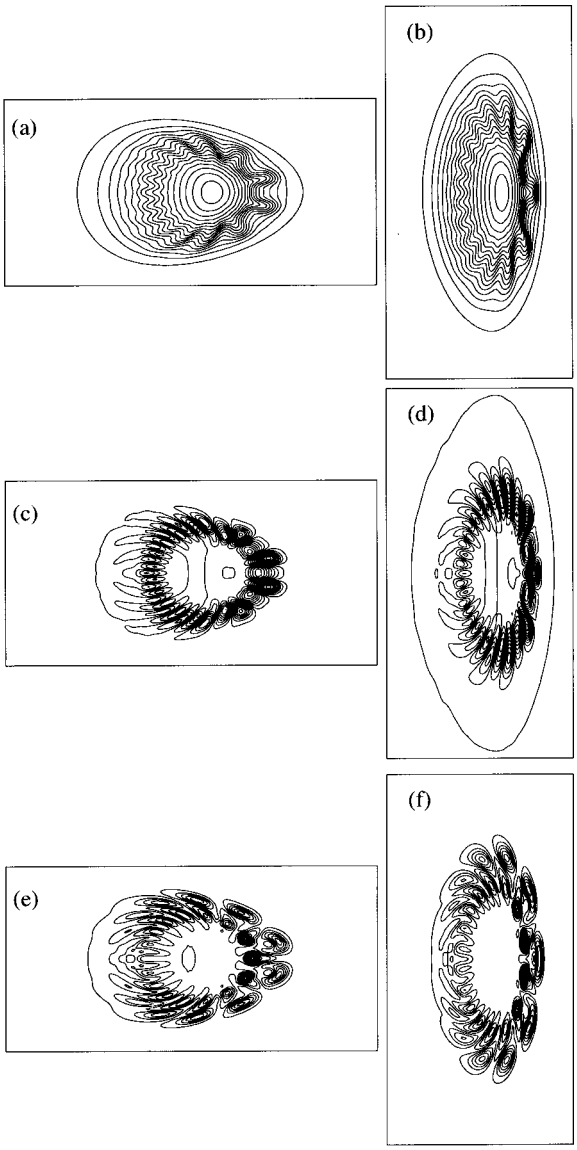

FIG. 4. Pressure contours on horizontally and vertically elongated poloidal sections at $t=200\tau_A$ are shown in (a) and (b), respectively. Contours of pressure fluctuations associated with (a) and (b) are shown in (c) and (d), respectively. Contours of pressure fluctuations at $t=400\tau_A$ are shown in (d) and (f), respectively.

contours (a ridge/valley structure) of the pressure grow toward the edge regions, especially on the outer side of the torus. In Figs. 4(e) and 4(f), contour plots of the amplitude of the pressure fluctuation at $t=400\tau_A$ are shown. We observe that contours are modulated strongly. At this stage of the time evolution, the energy growth is no longer exponential and eventually saturates by nonlinear effects, while the deformation is still dominated by the most unstable mode. An isosurface of the pressure at $t=400\tau_A$ is seen in Fig. 1. It is clearly seen that ridges of the pressure isosurface grow strongly toward the outer side of the torus, while the ridges in the inner side of the torus remain quite small.

In order to look closely into the origin of the exponential growth and pressure deformations observed above, we conduct a survey on various values of the resistivity in a range $1\times10^{-6}\leqslant\eta\leqslant3.16\times10^{-4}$ by the medium-resolution com-

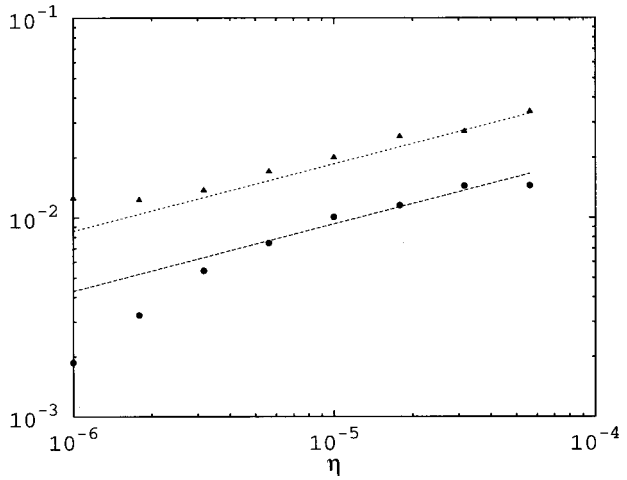

FIG. 5. Dependence of the growth rate of the excited mode on the resistivity η. The black triangles and circles are associated with the viscosity $\mu=1\times10^{-3}$ and 2×10^{-3}, respectively.

putations, for two values of the viscosity $\mu=1\times10^{-3}$ and 2×10^{-3}. In all of the simulations, the exponential growth of the kinetic energy and the wavy contours of the pressure on the outer side of the torus are observed. In Fig. 5, the growth rates are shown as a function of the resistivity. It is seen that the growth rate is almost proportional to $\eta^{1/3}$ both for the case of $\mu=1\times10^{-3}$ and 2×10^{-3}. Previous investigations[15,24] have shown that both resistive interchange and resistive ballooning instability bring growth rates proportional to $\eta^{1/3}$. Considering the pressure deformation observed in Figs. 4, these growths are identified to be caused by the resistive ballooning instability. [We have to keep in mind that linear analysis by Depassier and Cooper[24] is based on a large-aspect-ratio expansion. Since the aspect ratio of the LHD is finite (6.5), we have to be careful to compare our results with their analysis.]

The poloidal mode number of the ballooning instability observed in these simulations is mainly $m=16$, which is identified by counting the number of ridges in the pressure contours, the number of local maxima in the amplitude of the pressure fluctuation, and the number of islands observed in Poincare plots of the magnetic field lines. (Recall that the ballooning mode structure is realized by a coupled set of poloidal modes when it is described in the Fourier space.[25]) Since the excitation of the ballooning mode is first observed around the region $\iota/2\pi\simeq2/3$, where the pressure gradient becomes the steepest, the toroidal mode number is identified to be $n=10$, which is the smallest toroidal number available in our simulations. Under the value of the shear viscosity we used, modes with poloidal numbers much greater than $m=16$ are suppressed. We observed little dependence of the number of these ridges in the pressure contours, or the poloidal mode number of the most unstable mode, on the resistivity.

Now we pay attention to the growth rates associated with $\eta\leqslant1.78\times10^{-6}$ in Fig. 5. Some of the growth rates in this resistivity region do not obey the scaling $\eta^{1/3}$. We note two comments here. One is that growth rates with $\mu=1\times10^{-3}$ and $\eta<1\times10^{-6}$ give almost the same value with

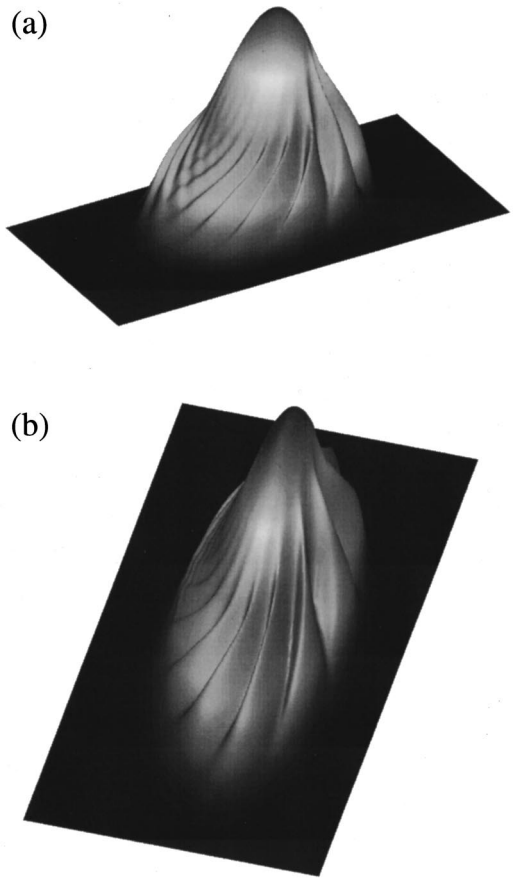

FIG. 6. Birds'-eye views of the pressure on (a) horizontally and (b) vertically elongated poloidal sections at $t=1000\tau_A$.

cases $\mu=1\times10^{-3}$ and $\eta=1\times10^{-6}$. We consider that a numerical dissipation caused by the finite difference scheme exceeds the physical effect of the resistivity for $\eta\leqslant1\times10^{-6}$. Then the effective value of the resistivity should be greater than 1×10^{-6} even when η is set smaller than 1×10^{-6}, to cause the larger value of the growth rate than the value expected by the $\eta^{1/3}$-scaling. Another comment is on the growth rate for cases $\mu=2\times10^{-3}$ and $\eta\leqslant1.78\times10^{-6}$. Their small growth rates lead the plasma to the long exposure under conductive effects and ohmic heating during the period of the formation of the eigenfunction, as observed in Fig. 3. We deduce that exposure by the nonideal dissipation effects for sufficiently long period causes change of the equilibrium and brings departure of the growth rate from the $\eta^{1/3}$-scaling.

B. Nonlinear deformation of the pressure profile

Next we see deformation of the pressure after the nonlinear saturation of the kinetic energy observed in Fig. 3. Again we concentrate on the higher-resolution computation with $\eta=3.16\times10^{-6}$ and $\mu=2\times10^{-3}$.

In Figs. 6(a) and 6(b), bird's-eye views of the pressure on the horizontally and vertically elongated poloidal sections at $t=1000\tau_A$ are shown, respectively. It is clearly observed that the ridges in the deformed pressure structure are twined around the core part of a confined plasma. It looks as if these

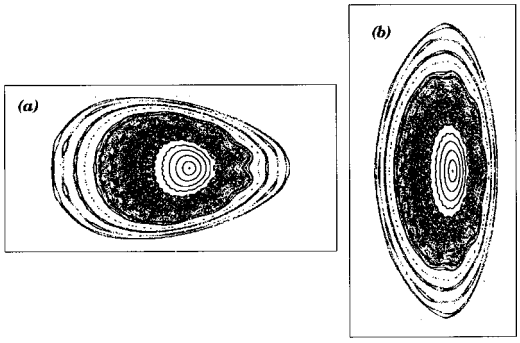

FIG. 7. Poincare plots of the magnetic field lines on (a) the horizontally and (b) vertically elongated poloidal sections.

ridges are growing toward the radial direction of a magnetic coordinate.[6] These ridges are formed in the period of the growth of the kinetic energy. Their shapes remain almost unchanged after the nonlinear saturation. A detailed comparison of the pressure profile at the time of the saturation ($t=520\tau_A$, figure is omitted) and that in the decay stage $t=1000\tau_A$, however, reveals that the pressure gradient tends to be less steep in the decay stage, especially on the inner side of the torus.

Influence of the nonlinear evolution on the plasma confinement is shown in Figs. 7 by the Poincare plots of the magnetic field lines on the horizontally and vertically elongated poloidal sections at $t=1000\tau_A$. The magnetic field lines are stochastic in the steep pressure gradient region due to the growth of the mode. The overall pressure profile is flattened in the stochastic field region. Clear magnetic surfaces remain at the center region of the plasma, however. The plasma is still well confined inside the nested magnetic surfaces. It is also observed that remains of magnetic surfaces are still in their clear shapes on the edge region of the plasma. These results show that the plasma evolution observed here is not very destructive.

In order to identify a physical mechanism which dominates these pressure deformations, we investigate the pressure budget equation

$$\frac{d}{dt}\int p\,d^3\mathbf{x}=-\int\frac{\partial pV_j}{\partial x_j}d^3\mathbf{x}-\int(\gamma-1)p\frac{\partial V_j}{\partial x_j}d^3\mathbf{x}-(\gamma-1)\times\int\frac{\partial}{\partial x_j}\left(-\kappa\frac{\partial}{\partial x_j}\frac{p}{\rho}\right)d^3\mathbf{x}+(\gamma-1)\times\int\Phi\,d^3\mathbf{x}+(\gamma-1)\int\eta J_jJ_j\,d^3\mathbf{x}. \tag{12}$$

Here $\int d^3\mathbf{x}$ represents the volume integral over the half-pitch period of the LHD torus.

Shown in Figs. 8 is the profile of the integrand in each term of the right-hand side of Eq. (12) observed on the horizontally elongated poloidal section at $t=520\tau_A$, namely, (a) the pressure flow, (b) the compression, (c) the thermal conduction, (d) the viscous heating, and (e) the Ohmic heating. In Figs. 8(a) through 8(e) plotted in bird's-eye view, the same level of normalization is used to compare the amplitude of each term. The horizontal plane corresponds to the zero

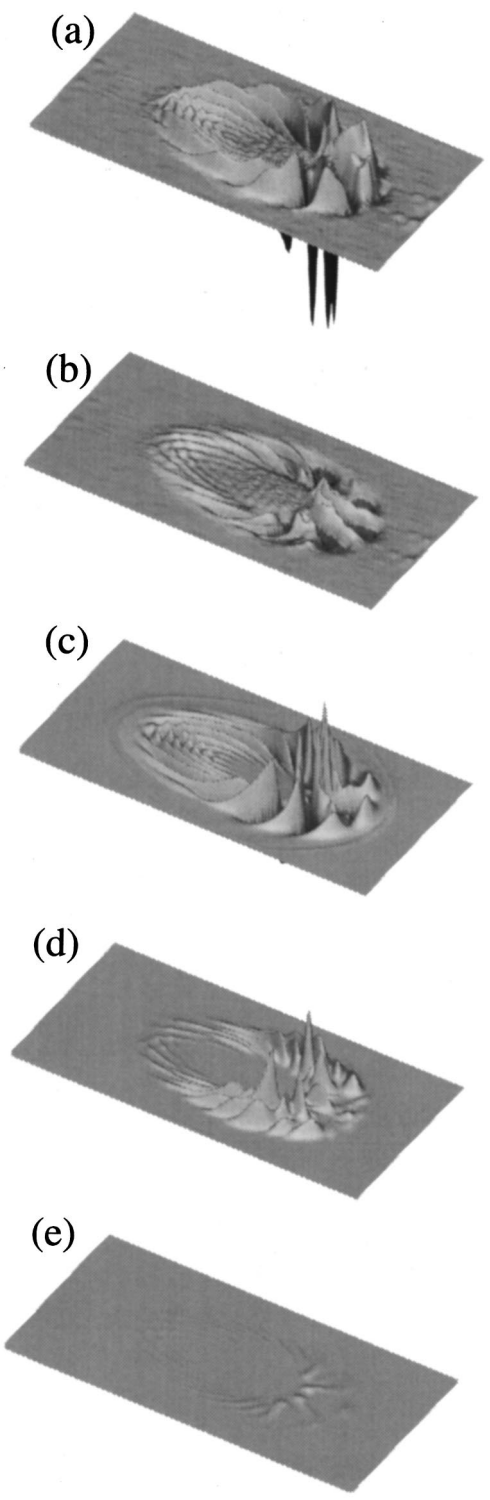

FIG. 8. Birds'-eye views of the profile of the (a) pressure flow, (b) compression, (c) thermal conduction, (d) viscous heating, and (e) Ohmic heating terms in the pressure budget equation on the horizontally elongated poloidal section at $t=520\tau_A$.

level, and regions with negative value are expressed by dark gray. In the estimation of the net pressure balance by the volume integration, contributions from the positive and negative parts are almost cancelled out to each other for the pressure flow, the compressibility and the thermal conduction terms, respectively. Thus the greatest part of the net balance in the pressure budget, or the net increase in the total pressure energy, is attributed to the viscous heating. Compared with the initial equilibrium, the increase in the total pressure energy is about 5% at $t=500\tau_A$. Since the viscous heating term is a second-order term as for the velocity, the predominant contribution on the net balance can be considered as a direct outcome of nonlinearity. Nonlinearity is revealed also in the profile of the Ohmic heating, which has the nature of a positive definite. Compared with the viscous heating term, however, the contribution of the Ohmic heating term on the net balance is observed to be significantly smaller, less than one-tenth of the contribution of the viscous heating, throughout the evolution of the process.

The local contribution of these terms can be examined more closely by the profiles shown in Figs. 8. It is observed that the pressure flow is the dominant term in the overall magnitude, and shows almost the same behavior with the structure of the pressure fluctuation. Namely, it takes a positive value at the pressure ridges and a negative value at the pressure valleys. On the other hand, all other terms show out-phase behavior with the ridge/valley structure of the pressure fluctuation. Thus the pressure flow term is revealed to be the agent that forms the deformed pressure structure, while other terms act to suppress the deformations. The second dominant term up to the saturation of the growth is the compression term, where the overall absolute magnitude is about two-thirds of that of the pressure flow term. This suggests the importance of the nature of compressibility in the evolution of the ballooning mode. As is shown in Fig. 8, the suppression effects of the thermal conduction and the viscous heating are also significant. The thermal conduction term becomes the second dominant after the saturation of the growth. It takes a large value at the sides of the pressure ridges and valleys, where the pressure gradient is steep due to the nonlinear evolution. On the other hand, the viscous heating term reveals a peaked profile, in particular, at the deepest location in the pressure valleys. It acts to increase the pressure in valley regions and make the pressure gradient less steep there.

IV. CONCLUDING REMARKS

We have reported results of nonlinear simulation of an MHD plasma that is executed in the full three-dimensional geometry of the LHD system. In this paper, we focused on plasma behavior in the medium poloidal mode number range by imposing the sterallator symmetry boundary conditions in the toroidal direction. Growth and saturation of the resistive ballooning modes were observed. We found that the growth rate of the kinetic energy in the linear growth period were almost proportional to $\eta^{1/3}$.

In the nonlinear stages of our simulations, we observed the formation of a sharp ridge structure in the pressure profile. The formation of the ridge structure was investigated through the estimation of the right-hand side (RHS) of the pressure budget equation (12). It was shown that the local plasma deformations were driven by the pressure flow term and suppressed mainly by the compression, viscous heating

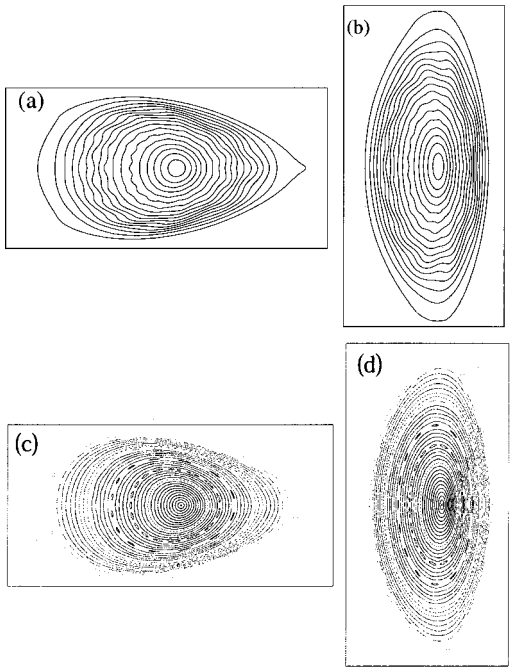

FIG. 9. An equilibrium reached by the plasma as a result of the pressure-driven relaxation. Contour plots of the pressure are shown on the (a) horizontally elongated poloidal section, and (b) vertically elongated poloidal section. Poincare plots of the magnetic field lines are shown on the (c) horizontally elongated poloidal section, and (d) vertically elongated poloidal section.

and thermal conduction terms. It is also noteworthy that the viscous heating term contributes much more to the net pressure increase than the ohmic heating.

In the description of Figs. 6, we noted that pressure deformations on the inner side of the torus were becoming smaller. We have also seen in Figs. 7 that the instability observed in this article is not so destructive. Since the kinetic energy decays monotonically after $t=520\tau_A$, it may suggest a transition of the plasma to a new equilibrium state. In order to examine this tendency, we conducted a very long simulation with the medium resolution, the resistivity and viscosity being the same with the higher-resolution simulation shown in the previous section. Contour plots of the pressure and Poincare plots of the magnetic field lines on the horizontally and vertically elongated poloidal sections at $t=4000\tau_A$ are shown in Figs. 9. We observe that the pressure profile is well-shaped and much broader than the initial profile. The magnetic surfaces are recovered clearly in Figs. 9, although the stored total pressure energy is increased more than 10% compared with the initial equilibrium. As far as the general tendency is concerned, the result that the broad pressure profile is spontaneously realized is consistent with observation in the actual LHD experiments, in which the plasma pressure usually reveals broad profile.[26] Although a computation with finer resolutions may be required to confirm such a long time scale behavior, the equilibrium shown in Figs. 9 is a state that is recovered from the midway disordered state. It can be viewed as a state that the plasma reaches as a result of nonlinear relaxation processes through redistribution of the plasma pressure. Since the pressure-driven instability appears in helical plasmas in its pure nature, they are considered to be a good target for studying the traits of pressure-driven relaxation. One direction in the extension of the present approach of computation may be to extract a guiding principle that governs such a pressure-driven relaxation process. Such a principle, if any, can also be applied to other configurations, like the tokamak.

ACKNOWLEDGMENTS

One of the authors (H.M.) would like to acknowledge his thanks to Dr. Nakajima, Dr. Sugama, Dr. Ichiguchi, Dr. Kanno, and Dr. T-H. Watanabe in NIFS and Professor W. A. Cooper in Ecole Polytechnique Federale de Lausanne for fruitful discussion. This simulation research was conducted by making use of the supercomputer NEC SX-4/64M2 in the theory and computer simulation center of NIFS.

This work was partially supported by a Grant-in-Aid for Scientific Research from the Ministry of Education, Culture, Sports, Science and Technology in Japan.

APPENDIX A: THE MHD EQUATIONS IN THE HELICAL-TOROIDAL COORDINATE SYSTEM

The MHD equations (1)–(7) are described in the helical-toroidal coordinate system Eqs. (8)–(10) as follows:

$$\frac{\partial \rho}{\partial t}=\frac{1}{\sqrt{g}}\frac{\partial(\sqrt{g}\rho v^i)}{\partial u^i}, \tag{A1}$$

$$\frac{\partial \rho v^i}{\partial t}=-g^{ih}\left[\frac{\partial T_h^k}{\partial u^k}+\left\{\begin{matrix}k\\ lk\end{matrix}\right\}T_h^l-\left\{\begin{matrix}l\\ hk\end{matrix}\right\}T_l^k+\epsilon_{ikh}j^k b^h\right] + \mu\left[-\frac{1}{\sqrt{g}}\epsilon_{ikh}\frac{\partial}{\partial u^k}\left(g_{hl}\frac{1}{\sqrt{g}}\epsilon_{lmn}\frac{\partial v^n}{\partial u^m}\right) + \frac{4}{3}\frac{\partial}{\partial u^i}\left\{\frac{1}{\sqrt{g}}\frac{\partial(\sqrt{g}v^i)}{\partial u^i}\right\}\right], \tag{A2}$$

$$T_i^k=\rho v^i v_k+p\,\delta_{ik}, \tag{A3}$$

$$\frac{\partial p}{\partial t}+v^i\frac{\partial p}{\partial u^i}=-\gamma p\frac{1}{\sqrt{g}}\frac{\partial(\sqrt{g}v^i)}{\partial u^i}+(\gamma-1)\left[\eta j^i j_i+\Phi + \kappa\frac{1}{\sqrt{g}}\frac{\partial}{\partial u^i}\left(\sqrt{g}\frac{\partial}{\partial u_j}\frac{p}{\rho}\right)\right], \tag{A4}$$

$$\frac{\partial b^i}{\partial t}=-e_{ikh}\frac{1}{\sqrt{g}}\frac{\partial}{\partial u^k}(-\sqrt{g}\epsilon_{hlm}v^l b^m+\eta j^h), \tag{A5}$$

$$j_i=\frac{1}{\sqrt{g}}\epsilon_{ikl}\frac{\partial b_l}{\partial u^k}, \tag{A6}$$

$$\Phi=2\mu\left[s_{ij}s_{ji}-\frac{1}{3}\left(\frac{1}{\sqrt{g}}\frac{\partial(\sqrt{g}\rho v^i)}{\partial u^i}\right)^2\right], \tag{A7}$$

$$s_{ij}=M_{ik}e_{kj}, \tag{A8}$$

$$\overline{\mathbf{M}} = \frac{\partial(u^1,u^2,u^3)}{\partial(x_1,x_2,x_3)}. \tag{A9}$$

Here g_{ij}, g^{ij}, and g are the (i,j)-components of covariant and contravariant components of the metric tensor and square of the Jacobian, respectively. The symbol

$$\left\{ \begin{matrix} h \\ ij \end{matrix} \right\} = \left\{ \begin{matrix} h \\ ji \end{matrix} \right\} = \frac{1}{2} g^{hp} \left(\frac{\partial g_{ip}}{\partial u^j} + \frac{\partial g_{jp}}{\partial u^i} + \frac{\partial g_{ij}}{\partial u^p} \right) \tag{A10}$$

is the Christoffel symbol. Symbols v^i, b^i, and j^i represent ith contravariant components of the velocity, magnetic field, and current vectors, respectively, while variable with subscripts represent contravariant components which can be obtained by using the metric tensors g_{ij} or g^{ij}. The bold face symbol $\underline{\mathbf{M}}$ represents a 3×3 Jacobian tensor and its (i,j) components are represented by the symbol M_{ij}. In Eq. (A2), we have used the vector identity

$$\nabla^2 \boldsymbol{v} = \nabla(\nabla\cdot\boldsymbol{v}) - \nabla\times(\nabla\times\boldsymbol{v}) \tag{A11}$$

for ease of a mathematical expression of the the Laplacian of a vector $\boldsymbol{v}$. In Eq. (A4), we have also used the fact that the dissipative coefficients are isotropic constant.

APPENDIX B: SYMMETRY CONDITIONS IMPOSED ON THE MHD EQUATIONS

As was described in Sec. II, the stellarator symmetry is imposed in the toroidal direction of this system. The boundary conditions associated with the stellarator symmetry on the contravariant components of the magnetic field vector may be described as

$$b^1(u^1,u^2,\Delta u^3) = -b^1(u^1,-u^2,-\Delta u^3), \tag{B1}$$

$$b^2(u^1,u^2,\Delta u^3) = b^2(u^1,-u^2,-\Delta u^3), \tag{B2}$$

$$b^3(u^1,u^2,\Delta u^3) = b^3(u^1,-u^2,-\Delta u^3), \tag{B3}$$

on the poloidal section $\phi=0$ (vertically elongated poloidal section), and

$$b^1(u^1,u^2,\pi/M-\Delta u^3) = b^1(-u^1,u^2,\pi/M+\Delta u^3), \tag{B4}$$

$$b^2(u^1,u^2,\pi/M-\Delta u^3) = -b^2(-u^1,u^2,\pi/M+\Delta u^3), \tag{B5}$$

$$b^3(u^1,u^2,\pi/M-\Delta u^3) = b^3(-u^1,u^2,\pi/M+\Delta u^3), \tag{B6}$$

on the section $\phi=\pi/M$ (horizontally elongated poloidal section), where Δu^3 is the grid interval along the u^3 direction. Boundary conditions on the density, pressure, and velocity fields are determined so that the MHD equations (1)–(7) are invariant when the boundary condition is imposed on the magnetic field and described as

$$\rho(u^1,u^2,\Delta u^3) = \rho(u^1,-u^2,-\Delta u^3), \tag{B7}$$

$$p(u^1,u^2,\Delta u^3) = p(u^1,-u^2,-\Delta u^3), \tag{B8}$$

$$v^1(u^1,u^2,\Delta u^3) = v^1(u^1,-u^2,-\Delta u^3), \tag{B9}$$

$$v^2(u^1,u^2,\Delta u^3) = -v^2(u^1,-u^2,-\Delta u^3), \tag{B10}$$

$$v^3(u^1,u^2,\Delta u^3) = -v^3(u^1,-u^2,-\Delta u^3), \tag{B11}$$

on the poloidal section $\phi=0$, and

$$\rho(u^1,u^2,\pi/M-\Delta u^3) = \rho(-u^1,u^2,\pi/M+\Delta u^3), \tag{B12}$$

$$p(u^1,u^2,\pi/M-\Delta u^3) = p(-u^1,u^2,\pi/M+\Delta u^3), \tag{B13}$$

$$v^1(u^1,u^2,\pi/M-\Delta u^3) = -v^1(-u^1,u^2,\pi/M+\Delta u^3), \tag{B14}$$

$$v^2(u^1,u^2,\pi/M-\Delta u^3) = v^2(-u^1,u^2,\pi/M+\Delta u^3), \tag{B15}$$

$$v^3(u^1,u^2,\pi/M-\Delta u^3) = -v^3(-u^1,u^2,\pi/M+\Delta u^3), \tag{B16}$$

at $\phi=\pi/M$.

[1] O. Motojima, H. Yamada, A. Komori *et al.*, Phys. Plasmas **6**, 1843 (1999).
[2] H. Yamada, K. Y. Watanabe, S. Sakakibara *et al.*, Phys. Rev. Lett. **84**, 1216 (2000); N. Ohyabu, K. Narihara, H. Funaba *et al.*, *ibid.* **84**, 103 (2000).
[3] N. Mizuguchi, T. Hayashi, and T. Sato, Phys. Plasmas **7**, 940 (2000).
[4] J. M. Greene and J. L. Johnson, Phys. Fluids **4**, 875 (1961).
[5] M. Wakatani, *Stellarator and Heliotron Devices* (Oxford University Press, Oxford, 1998).
[6] K. Ichiguchi, Recent Res. Dev. Plasmas **1**, 101 (2000).
[7] N. Nakajima, Phys. Plasmas **3**, 4545 (1996); **3**, 4556 (1996); J. Chen, N. Nakajima, and M. Okamoto, *ibid.* **6**, 1562 (1999).
[8] R. L. Dewar, P. Cuthbert, and R. Ball, Phys. Rev. Lett. **86**, 2321 (2001).
[9] C. Schwab, Phys. Fluids B **5**, 3195 (1993).
[10] D. V. Anderson, W. A. Cooper, W. A. Merazzi, U. Schwenn, and R. Gruber, Supercomputer **8**, 32 (1991).
[11] R. G. Storer and H. J. Gardner, Comput. Phys. Commun. (in press).
[12] S. Sakakibara, H. Yamada, A. Ejiri *et al.*, J. Phys. Soc. Jpn. **63**, 4406 (1994).
[13] H. R. Strauss, Plasma Phys. **22**, 733 (1980).
[14] M. Wakatani, H. Shirai, and M. Yamagiwa, Nucl. Fusion **24**, 1407 (1984).
[15] K. Ichiguchi, Y. Nakamura, and M. Wakatani, Nucl. Fusion **31**, 2073 (1991).
[16] B. A. Carreras, V. E. Lynch, H. Zushi, K. Ichiguchi, and M. Wakatani, Phys. Plasmas **5**, 3700 (1998).
[17] H. Harafuji, T. Hayashi, and T. Sato, J. Comput. Phys. **81**, 169 (1989); T. Hayashi, A. Takei, and T. Sato, Phys. Fluids B **4**, 1539 (1992).
[18] T. Hayashi, Proceedings of the 3rd Australia–Japan Workshop on Plasma Theory and Computation (Robertson, 1995) Australia National University, Canberra, Vol. 26 (1995).
[19] P. J. Roache, *Computational Fluid Dynamics* (Hermosa, Albuquerque, NM, 1974).
[20] C. Canuto, M. Y. Hussaini, A. Quarteroni, and T. A. Zang, *Spectral Methods in Fluid Dynamics* (Springer-Verlag, New York, 1987).
[21] C. Birdsall and A. B. Langdon, *Plasma Physics via Computer Simulation* (McGraw-Hill, New York, 1985).
[22] K. Ichiguchi, N. Nakajima, M. Okamoto, Y. Nakamura, and M. Wakatani, Nucl. Fusion **33**, 481 (1993).
[23] S. P. Hirshman and D. K. Lee, Comput. Phys. Commun. **43**, 143 (1986).
[24] M. C. Depassier and W. A. Cooper, Phys. Fluids **29**, 1948 (1986).
[25] R. D. Hazeltine and J. D. Meiss, Phys. Rep. **121**, 1 (1985).
[26] M. Fujiwara, K. Kawahata, N. Ohyabu *et al.*, "Overview of LHD experiments," to appear in *Proceedings of the 18th Fusion Energy Conference*, Sorento, 2000 (International Atomic Energy Agency, Vienna).